

Article

Ultra-Stable Anode-Free Na Metal Batteries Enabled by Al₂O₃-Functionalized Separators

Han Wang ¹, Yiheng Zhao ², Jiaqi Huang ³, Lu Wang ², Canglong Li ² and Yuejiao Chen ^{2,*}

¹ School of Chemistry Key Laboratory of Bio-Inspired Smart Interfacial Science and Technology of Ministry of Education, Beihang University, Beijing 100191, China; by2327112@buaa.edu.cn

² State Key Laboratory of Powder Metallurgy, Central South University, Changsha 410083, China; 8204222816@csu.edu.cn (Y.Z.); 8204212003@csu.edu.cn (L.W.); 235602052@csu.edu.cn (C.L.)

³ Beijing Key Laboratory of Enze Biomass Fine Chemicals, College of New Materials and Chemical Engineering, Beijing Institute of Petrochemical Technology, Beijing 102617, China; 2023540084@bipt.edu.cn

* Correspondence: cyj.strive@csu.edu.cn

Abstract

The development of anode-free sodium metal batteries (AFSMBs) offers a promising pathway to achieve ultrahigh energy density and cost efficiency inherent to conventional sodium ion/metal batteries. However, irreversible Na plating/stripping and dendritic growth remain critical barriers. Herein, we demonstrate that separator engineering is a pivotal strategy for stabilizing AFSMBs. Through systematic evaluation of four separators—2500 separator (PP), 2325 separator (PP/PE/PP), glass fiber (GF), and an Al₂O₃-coated PE membrane, we reveal that the Al₂O₃-coated separator uniquely enables exceptional interfacial kinetics and morphological control. Na||Na symmetric cells with Al₂O₃ coated separator exhibit ultralow polarization (4.5 mV) and the highest exchange current density (1.77×10^{-2} mA cm⁻²), while the anode-free AlC-NFPP full cells retain 91.6% capacity after 150 cycles at 2C. Specifically, the Al₂O₃ coating homogenizes Na⁺ flux, promotes dense and planar Na deposition, and facilitates near-complete stripping with minimal “dead Na”. This work establishes ceramic-functionalized separators as essential enablers of practical high-energy AFSMBs.



Academic Editor: Teofilo Rojo

Received: 8 July 2025

Revised: 27 July 2025

Accepted: 30 July 2025

Published: 4 August 2025

Citation: Wang, H.; Zhao, Y.; Huang, J.; Wang, L.; Li, C.; Chen, Y. Ultra-Stable Anode-Free Na Metal Batteries Enabled by Al₂O₃-Functionalized Separators. *Batteries* **2025**, *11*, 297. <https://doi.org/10.3390/batteries11080297>

Copyright: © 2025 by the authors. Licensee MDPI, Basel, Switzerland. This article is an open access article distributed under the terms and conditions of the Creative Commons Attribution (CC BY) license (<https://creativecommons.org/licenses/by/4.0/>).

1. Introduction

The relentless pursuit of sustainable energy storage solutions has intensified focus on Na-based batteries as a cost-effective alternative to lithium-based systems, leveraging the earth-abundance and geographical ubiquity of Na [1–6]. As shown in Figure 1, conventional sodium-ion batteries (SIBs), utilizing intercalation anodes (e.g., hard carbon), offer compelling safety and low-cost advantages due to the absence of metallic Na handling and manufacturing processes. However, their energy density remains fundamentally constrained by the limited capacity of intercalation materials. Sodium metal batteries (SMBs), which replace the intercalation anode with a Na metal foil, deliver significantly higher theoretical energy density by exploiting Na’s high specific capacity (1166 mAh g⁻¹) and low redox potential [7–9]. While maintaining favorable cost potential, SMBs face severe safety challenges stemming from the high reactivity of metallic Na and uncontrolled dendritic growth during cycling, leading to internal short circuits and thermal runaway [7,10,11].

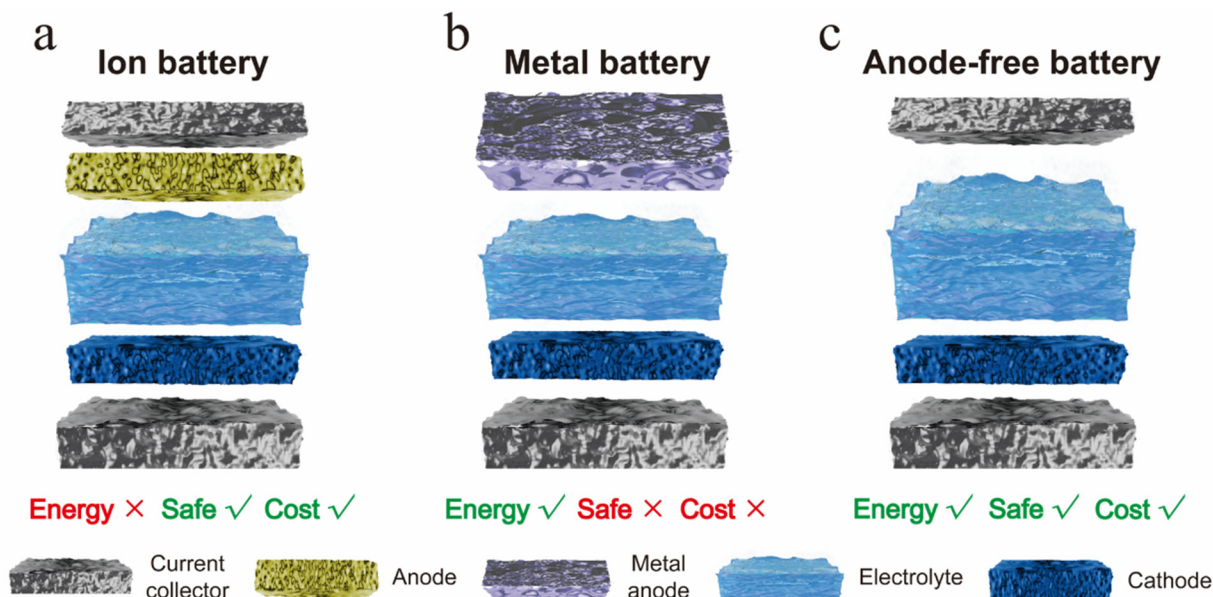


Figure 1. Schematic of the ion battery, metal battery, and anode-free battery configurations and the advantages and disadvantages of them.

Anode-free sodium metal batteries (AFSMBs) represent a transformative design strategy that addresses the trilemma of energy density, safety, and cost [10]. By eliminating the initial metallic Na anode and instead plating Na *in situ* directly onto the current collector during charging, AFSMBs achieve the ultimate energy density for Na-based systems (utilizing only the Na inventory pre-loaded in the cathode). This architecture simultaneously reduces material costs and mitigates hazards associated with handling reactive Na metal foils during manufacturing, offering a potential pathway to enhanced safety compared to conventional SMBs. Nevertheless, the practical realization of high-rate and long-cycling AFSMBs is impeded by the irreversibility of Na plating/stripping, exacerbated by heterogeneous Na deposition, unstable solid electrolyte interphase (SEI) formation, and rapid depletion of the finite Na inventory [12].

While electrolyte formulation and current collector design have been widely investigated to stabilize Na deposition [13,14], the separator, a critical yet often overlooked component, plays a decisive role in dictating ion transport uniformity, local current density distribution, electrolyte wetting/retention, and mechanical resilience against dendrites [15,16]. Its intrinsic properties (porosity, tortuosity, wettability, mechanical strength, chemical stability) profoundly influence the spatial homogeneity of Na^+ flux, nucleation behavior, and interfacial stability, thereby directly impacting Coulombic efficiency (CE), cycle life, and safety [17–19].

Herein, we present a rigorous comparative study elucidating the profound impact of separator selection on the electrochemical performance and interfacial stability of AF-SMBs. Four distinct separators, chosen for their diverse physicochemical characteristics, are systematically evaluated: widely used polyolefin membranes (2500 separator, monolayer PP; 2325 separator, trilayer PP/PE/PP), glass fiber (GF), and a customized Al_2O_3 -coated separator (PE coated with a uniform Al_2O_3 layer). Through comprehensive electrochemical characterization and detailed post-mortem analysis, we demonstrate that the separator choice critically governs key performance indicators. Strikingly, $\text{Na} \parallel \text{Na}$ symmetric cells employing the Al_2O_3 -coated separator exhibit exceptional interfacial stability, maintaining an ultralow polarization voltage of 4.5 mV over extended cycling, significantly outperforming cells using the 2500 separator, 2325 separator, or GF separators. More importantly, in practical anode-free AlC-NFPP full cells (Al foil coated with carbon particles ||

$\text{Na}_4\text{Fe}_3(\text{PO}_4)_2\text{P}_2\text{O}_7$), the Al_2O_3 -coated separator enables unprecedented cycling stability, delivering a remarkable 91.6% capacity retention after 150 cycles at a high rate of 2C. This superior performance is attributed to the Al_2O_3 coating enhancing electrolyte affinity, homogenizing Na^+ flux, and promoting dense and planar Na deposition. Our work unequivocally establishes separator engineering as a paramount strategy for unlocking the high-energy-density, safe, and cost-effective promise of anode-free Na metal batteries.

2. Experimental Section

Fabrication of Al_2O_3 -Coated Separator: The Al_2O_3 -functionalized PE separator was synthesized as follows: A homogeneous slurry was formulated by dispersing alumina nanoparticles (Al_2O_3 , 80 wt%), polyvinylidene fluoride binder (PVDF, 10 wt%), and N-methyl-2-pyrrolidone solvent (NMP, 10 wt%) via magnetic stirring (30 min) followed by ultrasonication (2 h). This slurry was uniformly deposited onto a pristine polyethylene (PE) substrate using a coating machine (MSK-AFA-W500-AL) set at a 5 μm gap height and 5 m/min coating speed. The composite membrane underwent sequential drying: 80 °C for 2 h in air, then 120 °C overnight under vacuum to eliminate solvent residues. Finally, the separator was calendared at 1 MPa to ensure robust mechanical integrity and interfacial cohesion.

Fabrication of NFPP Cathode: Commercial NFPP powder, polyvinylidene fluoride binder (PVDF), and carbon black conductor were homogenized in N-methyl-2-pyrrolidone (mass ratio: 95.5:1.5:3) to form a slurry. This slurry was coated onto Al foil using a coating machine, dried at 80 °C (12 h), then vacuum-dried at 120 °C (8 h) to yield electrodes with precise NFPP loading of $16.9 \pm 0.3 \text{ mg cm}^{-2}$. Circular cathodes (11 mm diameter) were punched for cell assembly.

Electrochemical Testing: All CR2032 coin cells were assembled in an Ar-filled glovebox (<0.01 ppm $\text{H}_2\text{O}/\text{O}_2$). Anode-free full cells paired AlC current collectors with NFPP cathodes (16.9 mg cm^{-2} loading) using 50 μL of electrolyte (1 M NaPF_6 in diglyme) and the tested separators. Galvanostatic cycling was performed at 1C and 2C rates (1C = 129 mA g⁻¹ NFPP). Symmetric $\text{Na}||\text{Na}$ cells utilized two Na disks (16 mm diameter), 50 μL of electrolyte, and the tested separators, cycled at 1 mA cm^{-2} and 1 mAh cm^{-2} . All cycling used a NEWARE tester (CT-4008Tn-5V50mA-HWX-U). Electrochemical impedance spectroscopy (EIS: 100 kHz–0.01 Hz, 5 mV amplitude) and Tafel analysis were conducted on an Ivium-n-Stat workstation.

Materials Characterization: Na deposition morphologies were examined using field-emission SEM (FE-SEM, TESCAN MIRA) on disassembled AlC current collectors. Residual Na distribution post-stripping was quantified via a CAIKON optical microscope (DMM-900C). Specifically, SEM analysis was conducted on AlC current collectors from anode-free full cells cycled at 1C for 50 cycles, disassembled in a charged state (with Na plated) inside an Ar-filled glovebox. Samples were rinsed with diglyme to remove leftover electrolyte, transferred in airtight containers, and imaged using a 5 kV electron beam to avoid damaging the Na deposits. For optical microscopy characterization, AlC current collectors were retrieved from anode-free full cells after 50 cycles at 1C, disassembled in a discharged state (post-Na stripping) within an Ar-filled glovebox. These samples were treated identically—rinsed with diglyme to eliminate residual electrolyte, transferred in airtight containers to prevent air exposure, and imaged under the optical microscope to analyze the distribution of residual Na.

3. Results and Discussion

First, we commence with a systematic electrochemical evaluation of Al-NFPP full cells employing four distinct separator architectures. As quantified in Figure 2a, cells with

the Al_2O_3 -coated separator demonstrate exceptional cycling stability at 1C, sustaining 85.9 mAh g^{-1} specific capacity over 150 cycles—a retention of 93.4% relative to initial capacity. This performance coincides with remarkably stable CE averaging 99.8%, indicative of highly reversible Na plating/stripping with minimal parasitic electrolyte decomposition. The 2500 separator shows progressive capacity fade, declining to 75.7 mAh g^{-1} by 150 cycles, suggesting gradual interfacial degradation. In stark contrast, the 2325 undergoes catastrophic failure, losing >95% capacity within 30 cycles, while the GF separator exhibits continuous capacity decay accompanied by CE deterioration. Remarkably, the Al_2O_3 -coated separator maintains superiority under aggressive 2C charging (Figure 2b), retaining 91.6% capacity with stable CE over 150 cycles. This robustness underscores its exceptional high-rate capability, attributed to the coating's role in homogenizing Na^+ flux and suppressing dendritic growth. Conversely, both 2325 and 2500 separators experience near-complete capacity collapse within 25 cycles, while GF delivers only 51.2% retention with severe CE oscillations, clear evidence of kinetic limitations, and irreversible Na inventory loss. Critical insights emerge from voltage capacity profiles (Figure 2c,d). The Al_2O_3 -coated separator maintains smooth, low-polarization curves throughout cycling, reflecting stable interfacial kinetics and minimal resistance growth. Even in the 100th cycle, its voltage hysteresis remains virtually unchanged, confirming durable electrode compatibility. Conversely, GF separators develop pronounced voltage fluctuations and increasing polarization, signaling cumulative interfacial deterioration and rising charge transfer resistance. The 2325 and 2500 separators exhibit even more severe degradation and all develop erratic voltage oscillations and capacity truncation. Collectively, these results establish the Al_2O_3 -coated separator as uniquely capable of maintaining interfacial integrity across extended cycling.

The distribution of relaxation times (DRT) analysis of the impedance of the full cell at different states of charge (SOCs) was further conducted. DRT spectra derived from electrochemical impedance spectroscopy (EIS) reveal distinct relaxation processes governing interfacial kinetics across separators (Figure 3). The magnitude of the relaxation time distribution highlights the relative contribution of each electrochemical process, while the x-axis spans critical relaxation times (10^{-5} to 10 s). The DRT spectra universally exhibit a dominant peak in the medium-frequency region ($\tau \approx 0.001\text{--}0.1 \text{ s}$), corresponding to charge-transfer resistance at the electrode interfaces. Notably, both the 2500 and Al_2O_3 -coated separators show lower peak magnitudes than 2325 and GF, indicating reduced baseline impedance attributable to separator thickness. Critically, the Al_2O_3 -coated separator manifests a pronounced charge-transfer peak only at low SOC during initial Na nucleation, suggesting transient kinetic limitations at early plating stages. And this peak rapidly attenuates at higher SOC, signifying stabilized interfacial kinetics. In stark contrast, conventional separators exhibit escalating charge-transfer peaks at high SOC, reflecting progressive interfacial degradation driven by inhomogeneous Na plating. This morphology instability promotes parasitic electrolyte decomposition and resistive byproduct accumulation, impeding charge transfer and amplifying impedance.

To further investigate the reversibility of Na deposition/stripping on the current collector, Figure 4 presents the galvanostatic cycling performance of $\text{Na} \parallel \text{Na}$ symmetric cells employing the four investigated separators under 1 mA cm^{-2} and 1 mAh cm^{-2} . The voltage hysteresis, a direct indicator of interfacial resistance and polarization, exhibits significant divergence among the separators. Critically, cells utilizing the Al_2O_3 -coated separator demonstrate exceptionally stable cycling with the smallest and most consistent polarization voltage throughout the test, maintaining an ultralow hysteresis of approximately 4.5 mV. This minimal polarization signifies highly reversible Na plating/stripping kinetics and superior interfacial stability. In stark contrast, cells with the GF separator

display the largest voltage hysteresis, indicative of substantial interfacial resistance and inefficient Na^+ transport. Furthermore, the GF-based cell suffers catastrophic failure characterized by a sudden voltage drop to near zero volts at approximately 200 h of cycling, unambiguously signifying an internal short circuit induced by Na dendrite penetration. While the 2500 and 2325 separators show intermediate performance, their polarization voltages remain significantly higher than that achieved with the Al_2O_3 -coated separator. These results highlight the exceptional efficacy of the Al_2O_3 -coated separator in suppressing dendrite growth and ensuring stable, safe operation of Na metal interfaces.

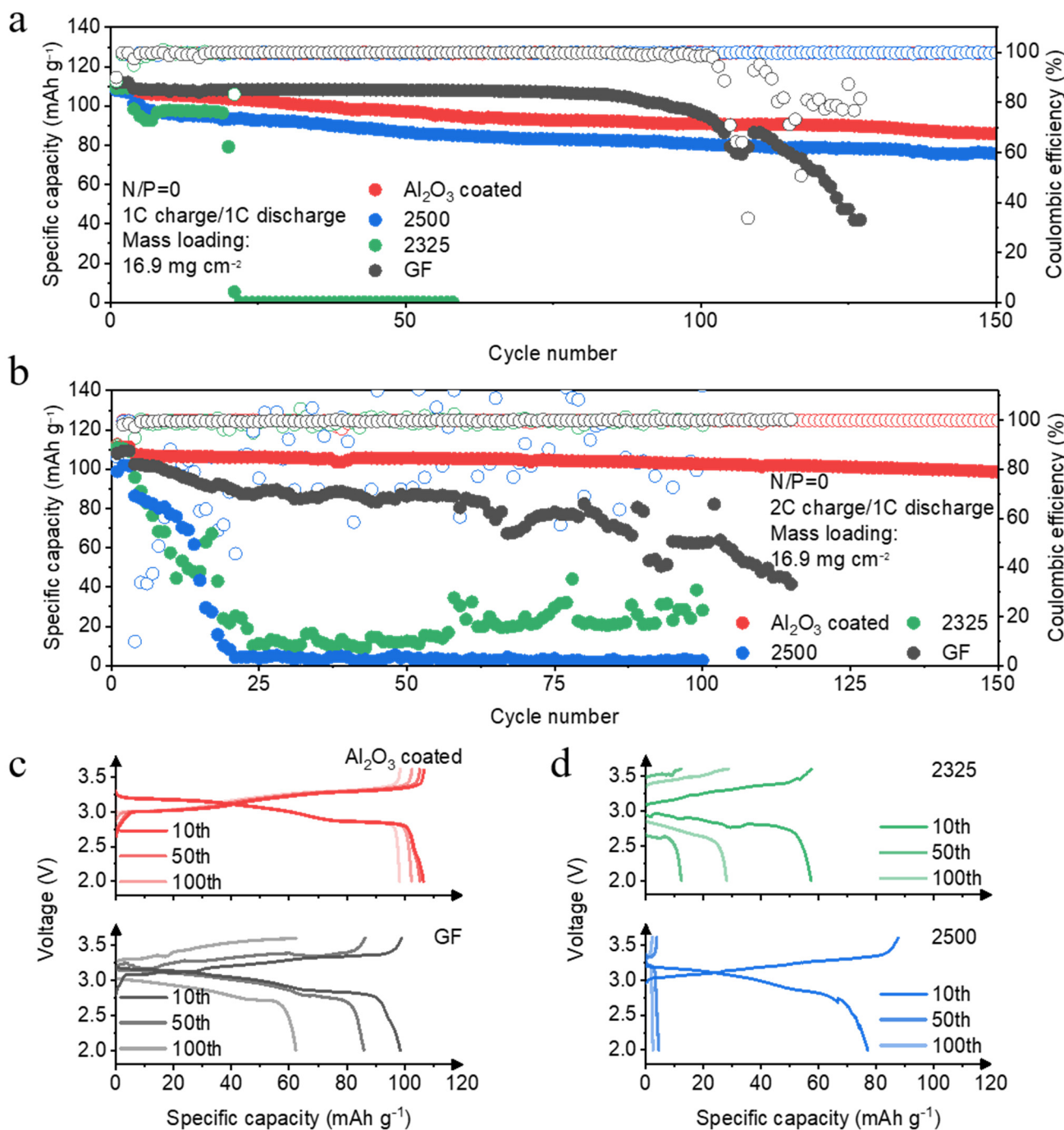


Figure 2. Electrochemical performance of anode-free full cells with different separators. (a) Long-term cycling stability at 1C charging. (b) Long-term cycling stability at 2C charging. (c,d) Corresponding voltage-specific capacity profiles at the 10th, 50th, and 100th cycles.

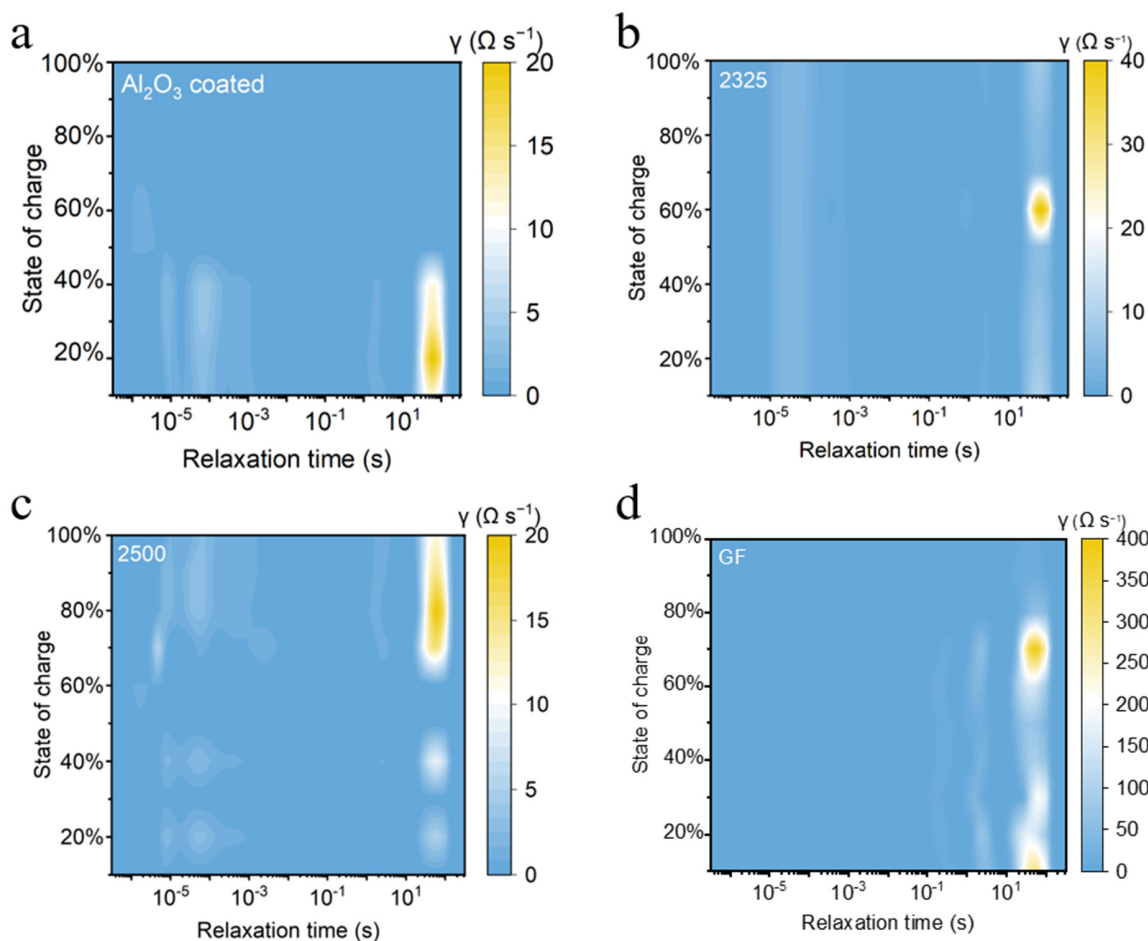


Figure 3. DRT analysis of interfacial charge-transfer kinetics in Al-NFPP anode-free Na batteries employing (a) Al_2O_3 -coated separator, (b) 2325 separator, (c) 2500 separator and (d) glass fiber separator across states of charge.

To elaborate on the differences in the aforementioned electrochemical performance under various separators, the EIS and DRT analyses of $\text{Na} \parallel \text{Na}$ symmetric cells integrated with four separators are presented in Figure 5. In the Nyquist plots (Figures 5a and S1 and Table S1), the charge-transfer resistance (R_{CT}) exhibits distinct differences across separators. The cell with the Al_2O_3 -coated separator displays the smallest semicircle diameter, corresponding to the lowest total interfacial resistance. To gain a more detailed insight, we performed DRT analysis (Figure 5b), where the Al_2O_3 -coated separator shows the lowest peak intensities for both R_{SEI} and R_{CT} , indicating highly efficient charge-transfer kinetics and a less resistive interfacial layer at the Na electrode [20]. Conversely, the GF-based cell presents the largest semicircle diameter in the Nyquist plot, signifying the highest interfacial resistance, which aligns with the DRT analysis showing the highest peak intensities for R_{SEI} and R_{CT} . The notably increased R_{SEI} and R_{CT} for the GF separator is consistent with its relatively large thickness, heterogeneous interfacial structure, and severe polarization observed during cycling (in line with prior cycle data). Cells utilizing 2500 and 2325 separators exhibit intermediate interfacial resistances in the Nyquist plots, with their DRT peak intensities for R_{SEI} and R_{CT} falling between those of Al_2O_3 -coated and GF separators. This is attributed to the fact that Al_2O_3 can enhance the wettability of the electrolyte to the anode, while increasing the electrolyte retention capacity of the separator. These combined EIS and DRT results provide mechanistic insights into how the Al_2O_3 -coated separator fosters superior plating/stripping reversibility and stability in Na metal systems.

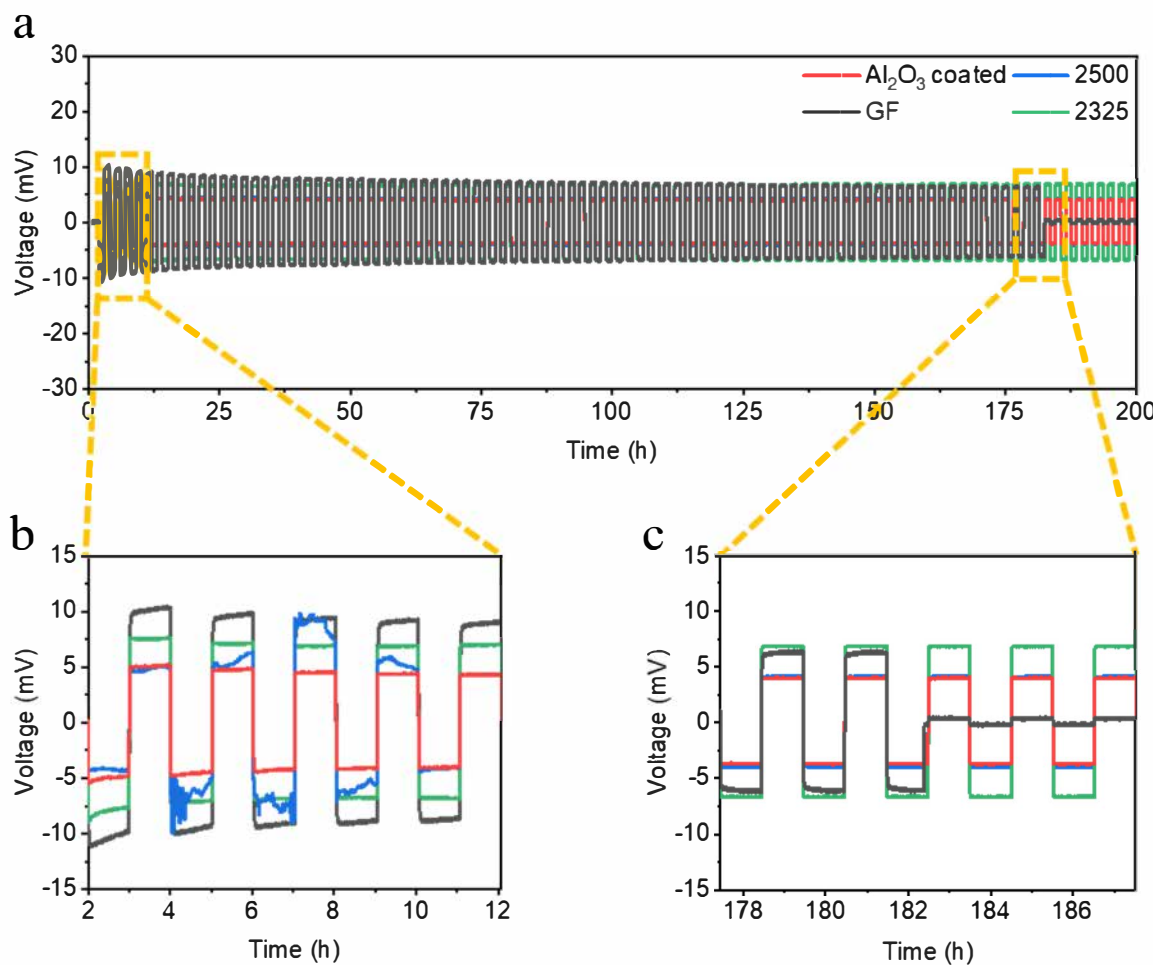


Figure 4. (a) Galvanostatic cycling (1 mA cm^{-2} , 1 mAh cm^{-2}) voltage profiles of $\text{Na} \parallel \text{Na}$ symmetric cells. (b) The enlarged voltage profiles from 2 to 12 h. (c) The enlarged voltage profiles from 177.5 to 187.5 h.

The interfacial Na^+ transport kinetics of different separators were investigated. Figure 5c presents Tafel polarization curves for $\text{Na} \parallel \text{Na}$ symmetric cells employing the four separators. The exchange current density (i_0), a fundamental parameter derived from the linear Tafel region and directly proportional to the rate of charge transfer at equilibrium, exhibits significant variation depending on the separator [21–23]. Strikingly, as showed in Table S2, the cell with the Al_2O_3 -coated separator achieves the highest exchange current density of $1.77 \times 10^{-2} \text{ mA cm}^{-2}$, significantly exceeding those measured for the other separators. This elevated i_0 unambiguously indicates significantly faster charge-transfer kinetics and lower activation energy barriers for the Na plating/stripping reactions at the interface facilitated by the Al_2O_3 -coated separator. In contrast, cells utilizing the GF separator yield the lowest exchange current density ($8.38 \times 10^{-3} \text{ mA cm}^{-2}$), reflecting the most sluggish interfacial kinetics, consistent with its high interfacial resistance observed in EIS and large polarization during cycling, which has been attributed to the large thickness of Na^+ in transport. The exchange current densities for the 2500 separator ($1.16 \times 10^{-2} \text{ mA cm}^{-2}$) and 2325 separator ($9.28 \times 10^{-3} \text{ mA cm}^{-2}$) fall between these extremes, aligning with their intermediate electrochemical performance. In addition, further Tafel slope calculations show the Al_2O_3 -coated separator has the lowest value (87.7 mV/dec), followed by 2500 PP (93.2 mV/dec), 2325 (98.5 mV/dec), and GF (111.6 mV/dec) (Figure S2). These Tafel analysis results quantitatively demonstrate that the Al_2O_3 -coated separator fosters the most favorable interfacial environment for rapid and efficient Na -ion charge transfer, providing

a kinetic rationale for its superior performance in promoting stable and reversible Na deposition. Meanwhile, we also measured the ionic conductivities of different separators (Figure 5d and Table S3). And the ionic conductivities of separators were determined via electrochemical impedance spectroscopy (EIS) using stainless steel as blocking electrodes (symmetrical cell: stainless steel || separator/electrolyte || stainless steel). Measurements were taken employing a 0.1–100 kHz frequency range with 10 mV amplitude at 25 °C. The bulk resistance (R_b) was extracted from the high-frequency intercept on the real axis in the Nyquist plots. Ionic conductivity (σ) was calculated as follows:

$$\sigma = \frac{d}{R_b \cdot S}$$

where d = separator thickness (μm), S = electrode area (cm^2), and R_b = bulk resistance (Ω).

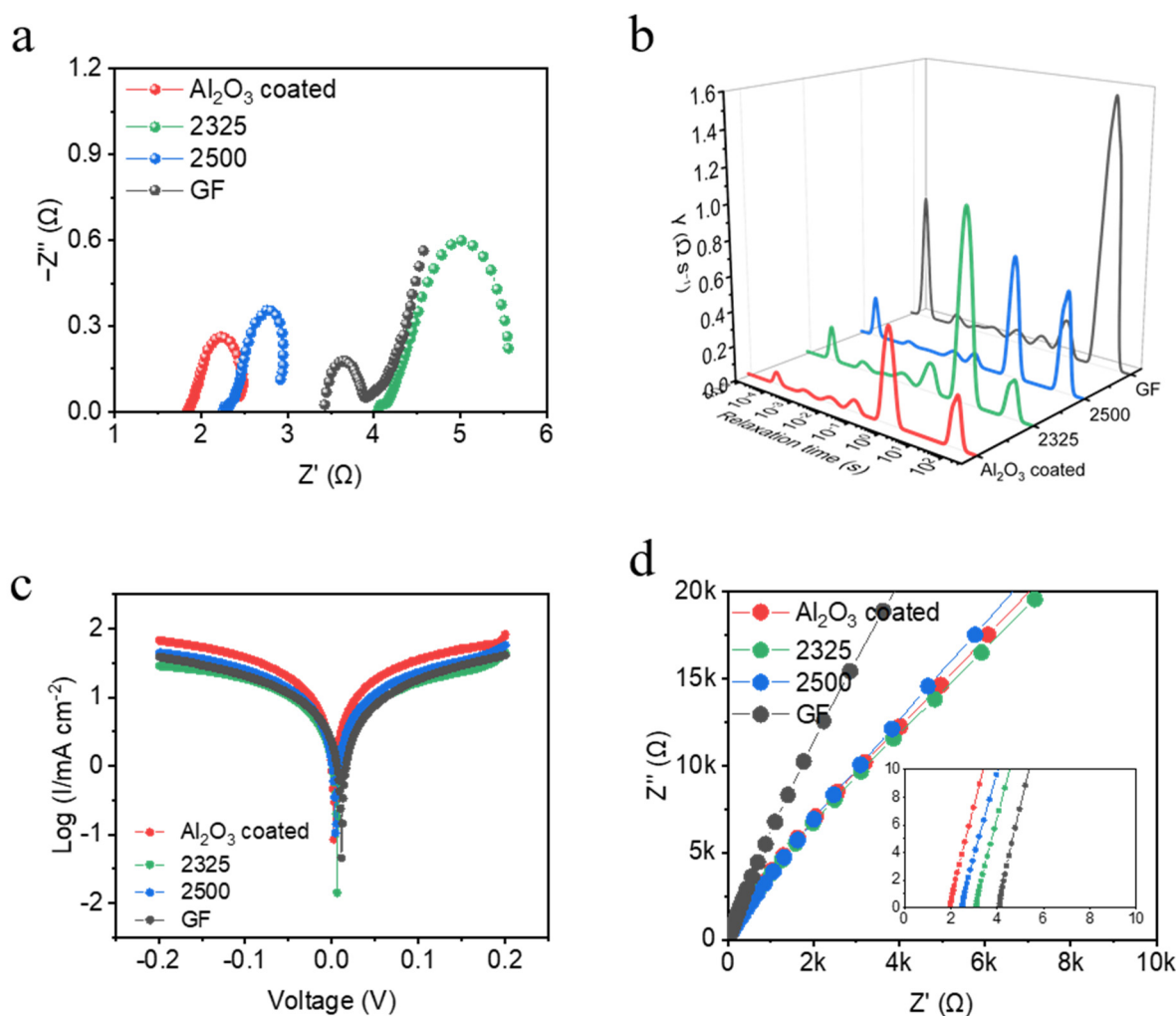


Figure 5. (a,b) EIS and the corresponding DRT analyses of different separators in symmetric Na-Na cells. (c) Tafel plots of different separators in symmetric Na-Na cells. (d) Nyquist plots of different separators in symmetric stainless steel–stainless steel cells.

The Al_2O_3 -coated separator exhibits the highest ionic conductivity ($9.19 \times 10^{-4} \text{ S cm}^{-1}$), significantly surpassing conventional polyolefin separators (2500: $6.52 \times 10^{-4} \text{ S cm}^{-1}$; 2325: $5.26 \times 10^{-4} \text{ S cm}^{-1}$) and exceeding glass fiber (GF: $7.91 \times 10^{-4} \text{ S cm}^{-1}$). This enhancement is attributed to the Al_2O_3 coating's superior electrolyte wettability, which facilitates rapid electrolyte infiltration, reduces interfacial resistance, and establishes continuous ion-transport pathways. The elevated ionic conductivity of the Al_2O_3 -coated

separator directly homogenizes the Na^+ transport, underpinning its exceptional electrochemical performance in anode-free sodium metal batteries. Furthermore, wettability tests were performed by depositing 1M NaPF_6 in G2 electrolyte onto the four separators (Figure S3). After 20 s, the Al_2O_3 -coated separator showed rapid, uniform electrolyte spreading, whereas 2325 and 2500 separators retained discrete droplets. Glass fiber wetted quickly but required excessive electrolyte, unfavorable for the energy density of the anode-free battery. This indicates the Al_2O_3 coating enhances electrolyte affinity, critical for ion transport and deposition behavior.

To elucidate the critical link between separator properties and Na deposition behavior, we directly characterized the morphology of deposited Na on AlC current collectors at a current density of 1C (Figure 6). Strikingly, SEM imaging reveals that the Al_2O_3 -coated separator enables the formation of an exceptionally dense, compact, and planar Na layer with minimal surface irregularities, indicative of highly uniform nucleation and growth that effectively suppresses dendrite initiation. Conversely, Na deposited using 2500, 2325, and GF separators exhibits severely heterogeneous, porous, and dendritic morphologies, featuring extensive mossy structures, sharp protrusions, and deep voids. Higher-magnification analysis further underscores this fundamental contrast. This undesirable porous morphology drastically increases the active surface area, accelerating parasitic electrolyte decomposition and unstable SEI formation, while simultaneously compromising mechanical cohesion, thereby promoting dendrite penetration and premature cell failure. The superior interfacial stability and cycling performance achieved with the Al_2O_3 -coated separator are thus directly attributable to this markedly denser and more homogeneous Na deposition morphology.

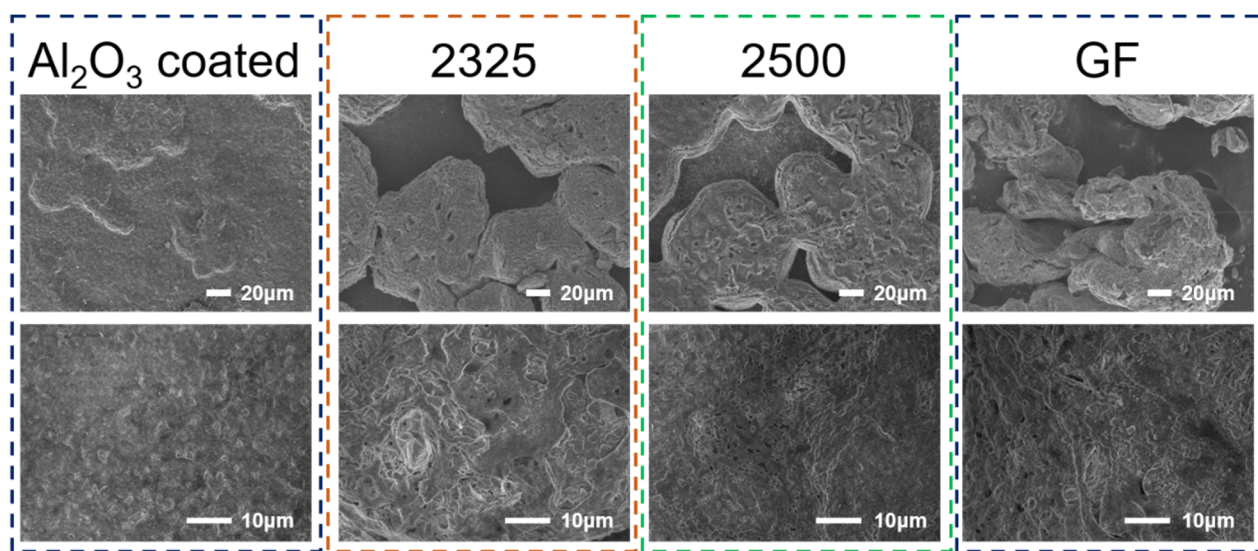


Figure 6. Top-view SEM images of Na deposition morphology on AlC current collectors after 50 cycles at 1C in anode-free full cells (charged state).

Optical microscopy analysis was further conducted on the AlC current collectors with stripping to evaluate the Na stripping reversibility and uniformity (Figure 7). Strikingly, the current collector cycled with the Al_2O_3 -coated separator exhibits minimal residual Na, appearing predominantly clean and uniform with only sparse, isolated traces of Na, indicative of highly efficient and near-complete stripping. In stark contrast, current collectors paired with 2500, 2325, and especially GF separators display extensive, heterogeneous patches of residual Na metal, signifying severely incomplete stripping and pronounced inhomogeneity. Alarmingly, the GF separator itself also exhibits copious macroscopic Na deposits adhering to its surface, directly evidencing catastrophic interfacial instability. This

substantial Na residue represents irreversible “dead Na,” permanently lost to the active inventory, accelerating capacity fade and contributing directly to the low CE and premature failure observed in cells using these separators. The exceptionally clean stripping enabled by the Al_2O_3 -coated separator provides direct visual confirmation of its superior interfacial compatibility and plating/stripping reversibility, underpinning its outstanding electrochemical performance.

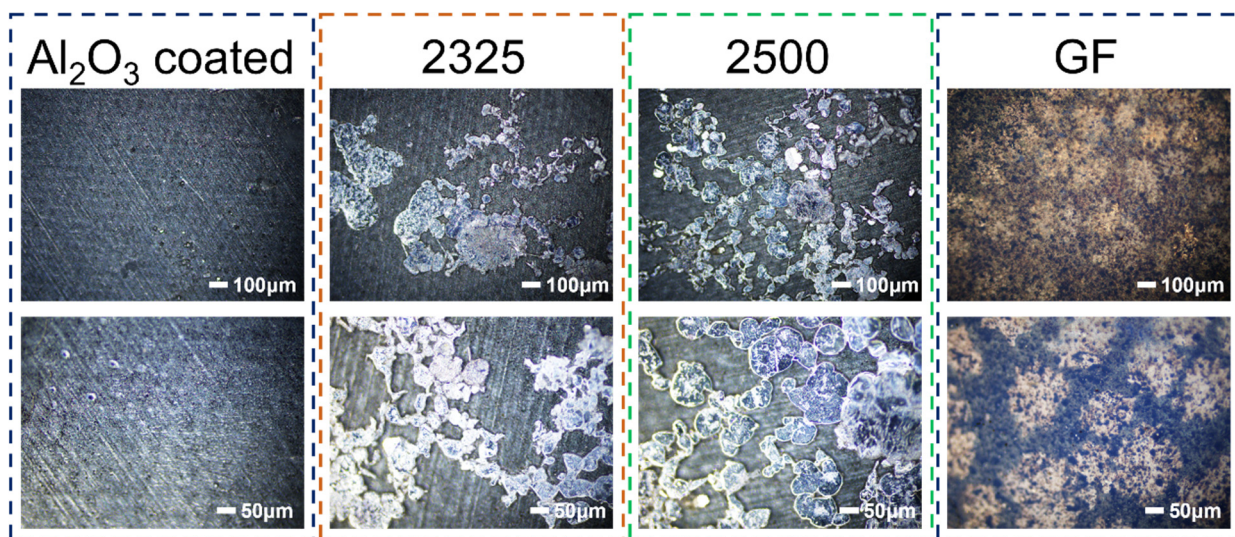


Figure 7. Optical microscopy of AlC current collectors after Na stripping. Top row: 10 \times magnification images showing macroscopic distribution of residual Na; bottom row: 20 \times magnification images revealing detailed morphology of remaining Na deposits.

4. Conclusions

This study unequivocally establishes that separator selection dictates the interfacial stability, Na deposition morphology, and ultimate viability of anode-free Na metal batteries. The Al_2O_3 -coated separator emerges as a superior candidate, fundamentally outperforming conventional polyolefin (2500 separator/2325 separator) and glass fiber membranes through four key mechanisms:

- ①. Kinetic Enhancement: Reduced interfacial resistance (EIS) and accelerated charge transfer ($1.77 \times 10^{-2} \text{ mA cm}^{-2}$) enable ultralow polarization (4.5 mV).
- ②. Morphological Control: Uniform Na^+ flux and enhanced electrolyte wetting foster dense, planar Na deposition, eliminating dendrites and voids.
- ③. Stripping Reversibility: Near-complete Na stripping minimizes “dead Na” residue on current collectors and separators, directly boosting CE.
- ④. Electrochemical Resilience: In full AlC-NFPP anode-free fill cells, the Al_2O_3 -coated separator achieves 91.6% capacity retention after 150 cycles at 2C.

These results resolve a critical materials challenge in AFSMBs by proving that ceramic coatings (e.g., Al_2O_3) on polyolefin separators can mitigate interfacial instability for stable cycling. Future efforts may prioritize multifunctional separator designs to realize the full energy density potential of anode-free configurations for sustainable energy storage.

Supplementary Materials: The following supporting information can be downloaded at: <https://www.mdpi.com/article/10.3390/batteries11080297/s1>, Figure S1. fitted EIS curves of different separators, Figure S2. Calculated Tafel slopes for different separators in Na-Na symmetric cells, Figure S3. Wettability tests of different separators. A liquid droplet was applied, with wetting states shown at 0 s (top) and 20s (bottom) to compare absorption behaviors, Table S1. RCT from the fitted

EIS, Table S2. Exchange current densities (i_0) derived from polarization curves, Table S3. Ionic conductivity derived from Nyquist plots.

Author Contributions: Conceptualization, H.W. and Y.C.; Methodology, Y.Z.; Software, C.L.; Validation, L.W.; Formal analysis, H.W. and J.H.; Investigation, J.H.; Writing—original draft, H.W.; Writing—review & editing, Y.C.; Visualization, L.W.; Supervision, Y.C.; Funding acquisition, Y.C. All authors have read and agreed to the published version of the manuscript.

Funding: This research was funded by the National Natural Science Foundation of China (No. 52377222) and Natural Science Foundation of Hunan Province (No. 2023JJ20064).

Data Availability Statement: Dataset available on request from the authors.

Conflicts of Interest: The authors declare that they have no known competing financial interests or personal relationships that could have appeared to influence the work reported in this paper.

References

1. Hu, Z.W.; Liu, L.Y.; Wang, X.; Zheng, Q.; Han, C.; Li, W. Current progress of anode-free rechargeable sodium metal batteries: Origin, challenges, strategies, and perspectives. *Adv. Funct. Mater.* **2024**, *34*, 2313823. [[CrossRef](#)]
2. Tang, F.; Yang, Y.; Liu, C.C.; Yang, S.; Xu, S.; Yao, Y.; Yang, H.; Yang, Y.; He, S.; Pan, H.; et al. Initially anode-free sodium metal battery enabled by strain-engineered single-crystal aluminum substrate with (100)-preferred orientation. *Nat. Commun.* **2025**, *16*, 2280. [[CrossRef](#)] [[PubMed](#)]
3. Chen, Y.J.; Ye, C.; Zhang, N.J.; Liu, J.; Li, H.; Davey, K.; Qiao, S.-Z. Prospects for practical anode-free sodium batteries. *Mater. Today* **2024**, *73*, 260–274. [[CrossRef](#)]
4. Petersen, D.; Gronenberg, M.; Lener, G.; Leiva, E.P.M.; Luque, G.L.; Rostami, S.; Paoletta, A.; Hwang, B.J.; Adelung, R.; Abdollahifar, M. Anode-free post-Li metal batteries. *Mater. Horiz.* **2024**, *11*, 5914–5945. [[CrossRef](#)]
5. Xie, C.L.; Liang, K.; Wu, H.; Xie, Z.; Ren, Y.; Dai, J.; Lu, J.; Tang, Y.; Wang, H. Revealing the formation mechanism of inactive sodium in anode-free sodium batteries: Crystal mismatch and weak lattice force. *Adv. Energy Mater.* **2025**, *15*, 2500351. [[CrossRef](#)]
6. Liu, J.-C.; You, T.; Zhao, Y.-F.; Liu, F.-Q.; Li, J.-D.; Wang, L.-L.; Wang, C.; Li, L. Multifunctional sulfonate additive induced CEI layer enables ultra-stable peo based solid-state sodium batteries. *Rare Met.* **2025**, *44*, 3817–3826. [[CrossRef](#)]
7. Huo, S.D.; Wang, L.; Su, B.; Xue, W.; Wang, Y.; Zhang, H.; Li, M.; Qiu, J.; Xu, H.; He, X. Anode-free li metal batteries: Feasibility analysis and practical strategy. *Adv. Mater.* **2024**, *36*, e2411757. [[CrossRef](#)]
8. Wu, N.; Shen, J.; Li, Q.; Li, S.; Guo, D.; Li, J.; Liu, G.; Zhao, J.; Cao, A.; Mi, H.; et al. Synergistic bimetallic interaction and regulated void size in isocubanite CuFe₂S₃ enables ultrafast and durable sodium storage. *ACS Sustain. Chem. Eng.* **2025**, *13*, 5546–5556. [[CrossRef](#)]
9. Zhao, J.; Yue, J.; Gao, S.; Li, T. Synergistic multi-element strategy enables snsbmnbite high-entropy alloy anode for stable and fast sodium storage. *ACS Sustain. Chem. Eng.* **2025**, *13*, 11143–11152. [[CrossRef](#)]
10. Zhou, Y.; Wang, P.; Wang, K.; Fang, X.; Li, W.; Nai, J.; Liu, Y.; Wang, Y.; Zou, S.; Yuan, H.; et al. Developing high-performance anode-free lithium batteries: Challenges, strategies, and opportunities. *Adv. Funct. Mater.* **2025**, *35*, 2424022. [[CrossRef](#)]
11. Zhang, H.; Bai, T.; Cheng, J.; Ji, F.; Zeng, Z.; Li, Y.; Zhang, C.; Wang, J.; Xia, W.; Ci, N.; et al. Unlocking the decomposition limitations of the Li₂C₂O₄ for highly efficient cathode prelithiations. *Adv. Powder Mater.* **2024**, *3*, 100215. [[CrossRef](#)]
12. Xiang, L.; Li, X.T.; Xiao, J.; Zhu, L.; Zhan, X. Interface issues and challenges for nasicon-based solid-state sodium-metal batteries. *Adv. Powder Mater.* **2024**, *3*, 100181. [[CrossRef](#)]
13. Huang, H.L.; Liu, C.; Liu, Z.Y.; Wu, Y.; Liu, Y.; Fan, J.; Zhang, G.; Xiong, P.; Zhu, J. Functional inorganic additives in composite solid-state electrolytes for flexible lithium metal batteries. *Adv. Powder Mater.* **2024**, *3*, 100141. [[CrossRef](#)]
14. Xu, J.; Jiang, J.B.; Tang, H.; Chen, Z.; Chen, J.; Zhang, Y.; Lee, C.-S. Interlayer engineering and electronic regulation of mose₂ nanosheets rolled hollow nanospheres for high-performance sodium-ion half/full batteries. *Adv. Powder Mater.* **2024**, *3*, 100169. [[CrossRef](#)]
15. Shao, A.; Wang, H.; Zhang, M.; Liu, J.; Cheng, L.; Li, Y.; Guo, Y.; Wang, Z.; Jia, Q.; Wang, X.; et al. Multiscale interfacial stabilization via prelithiation separator engineering for Ah-level anode-free lithium batteries. *Nat. Commun.* **2025**, *16*, 4145. [[CrossRef](#)] [[PubMed](#)]
16. Li, K.; Yang, W.; Hao, J.; Gong, Y. A “two-in-one” strategy in sodium metal batteries: A cost-effective Co/Mo metal–organic framework-modified filter paper separator with ion-sieving and desolvation effects in confined channels. *ACS Sustain. Chem. Eng.* **2025**, *13*, 10102–10118. [[CrossRef](#)]
17. Shi, R.J.; Jiao, S.L.; Yang, Z.R.; Bo, Z.; Jiao, J.; Zhao, Y. Regulating interfacial wettability for fast mass transfer in rechargeable metal-based batteries. *ACS Nano* **2025**, *19*, 8462–8508. [[CrossRef](#)]

18. Fan, Z.X.; Chen, X.Y.; Shi, J.J.; Nie, H.; Zhang, X.; Zhou, X.; Xie, X.; Xue, Z. Functionalized separators boosting electrochemical performances for lithium batteries. *Nano-Micro Lett.* **2025**, *17*, 128. [[CrossRef](#)]
19. Yuan, W.; Qu, X.; Wang, Y.; Li, X.; Ru, X.; Jia, D.; Zhao, L.; Hou, Y.; Shen, J.; Shen, Z.; et al. Polycationic polymer functionalized separator to stabilize aqueous zinc-iodine batteries. *Energy Storage Mater.* **2025**, *76*, 104130. [[CrossRef](#)]
20. Cai, X.; Zhang, C.P.; Ruan, H.J.; Chen, Z.; Zhang, L.; Sauer, D.U.; Li, W. Cross-scale decoupling kinetic processes in lithium-ion batteries using the multi-dimensional distribution of relaxation time. *Adv. Sci.* **2024**, *11*, e2406934. [[CrossRef](#)]
21. Wang, X.L.; Li, Y.; Liu, J.; Yang, S.J.; Hu, J.K.; Mai, W.Q.; Wen, R.; Yuan, H.; Huang, J.Q. A robust dual-layered solid electrolyte interphase enabled by cation specific adsorption-induced built-in electrostatic field for long-cycling solid-state lithium metal batteries. *Angew. Chem.-Int. Ed.* **2025**, *64*, e202421101. [[CrossRef](#)]
22. Park, J.B.; Choi, C.; Kim, M.S.; Kang, H.; Kwon, E.; Yu, S.; Kim, D.-W. Designing metal phosphide solid-electrolyte interphase for stable lithium metal batteries through electrified interface optimization and synergistic conversion. *Nano-Micro Lett.* **2025**, *17*, 315. [[CrossRef](#)]
23. Hobold, G.M.; Kim, K.-H.; Gallant, B.M. Beneficial vs. Inhibiting passivation by the native lithium solid electrolyte interphase revealed by electrochemical Li^+ exchange. *Energy Environ. Sci.* **2023**, *16*, 2247–2261. [[CrossRef](#)]

Disclaimer/Publisher's Note: The statements, opinions and data contained in all publications are solely those of the individual author(s) and contributor(s) and not of MDPI and/or the editor(s). MDPI and/or the editor(s) disclaim responsibility for any injury to people or property resulting from any ideas, methods, instructions or products referred to in the content.